Multiple-scattering EXAFS analysis

Jing Liu and Anatoly I. Frenkel*

Department of Materials Science and Chemical Engineering, Stony Brook University, 100 Nicolls Road, Stony Brook, NY 11794, USA. *Correspondence e-mail: anatoly.frenkel@stonybrook.edu

Advances in multiple-scattering theory play a key role in the ongoing progress of analysis and modelling methods of extended X-ray absorption fine structure (EXAFS). This chapter will focus on the history and development of the multiple-scattering theory, introduce data-analysis and modelling strategies that employ multiple-scattering contributions to EXAFS, and discuss their applications to a variety of systems.

1. Introduction

Single-scattering analysis of extended X-ray absorption fine-structure (EXAFS) spectroscopy limited researchers to the first and, rarely, the second nearest-neighbouring shells of atomic species around the X-ray absorbing atoms. The inability to 'peek' beyond the first shell is not much of a limitation for many systems, notably those that are strongly disordered and/or of low dimensionality, where only the first peak in r-space can be reliably analyzed. In the case of relatively ordered materials, in particular those possessing relatively open lattices [for example f.c.c. metals (Alayoglu *et al.*, 2009; Frenkel, 1999; Rehr & Albers, 1990), alkali halide salts (Frenkel *et al.*, 1993, 1995) and some perovskites with formula BX_3 (Balerna *et al.*, 1991; Kuzmin & Purans, 1993; Kuzmin *et al.*, 1993)], strong multiple-scattering contributions to EXAFS account for a large portion of the spectrum (Lee & Pendry, 1975; Rehr & Albers, 1990) and are comparable with single-scattering contributions. Therefore, multiple-scattering contributions have to be included in EXAFS calculations and analysis for reliable structural refinement beyond the first nearest-neighbouring shell whenever the experimental data quality allows such analysis. The role of multiple-scattering events has been the subject of extensive and long-term discussions, stimulating the development of theories and data-analysis techniques,

The multiple-scattering effect occurs when the photoelectron wave is scattered more than once by surrounding atoms before returning to the X-ray absorbing atom. Multiple-scattering (MS) paths differ in the number of legs and in the type of scattering geometry. For example, single-scattering paths have two legs. Double-scattering paths (for example MS1 and MS4–MS6 in Fig. 1) have three legs, and triple-scattering paths (MS2 and MS3 in Fig. 1) have four legs. Multiple-scattering paths are very important in the X-ray absorption near-edge structure (XANES) region, because in this region a photoelectron with low kinetic energy has a long mean free path that permits the contribution of extensive multiple-scattering events to the XANES structure (Penner-Hahn, 2001). Multiple-scattering paths can be extraordinarily important when the atoms are present in a linear or nearly
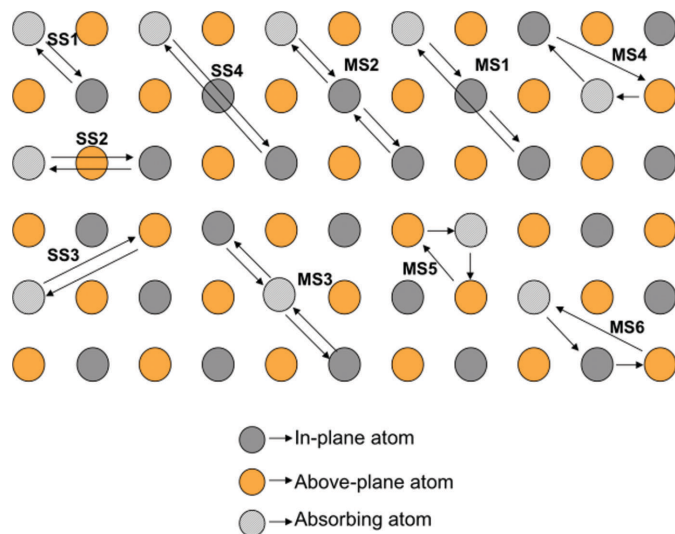

In-plane atom
Above-plane atom
Absorbing atom
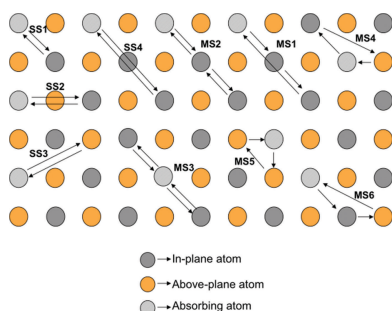
linear arrangement. We consider a three-atom (ABC) system (Teo, 1981; Teo & Lee, 1979) where a photoelectron is emitted from atom A and is scattered first by atom B and then by atom C before returning to atom A, as seen in Fig. 2 using oxygen as an example. The calculated scattering amplitude shows a dependence on the value of the angle β and the wavenumber k. For all k values, the scattering amplitude at atom B reaches a maximum of $F \simeq 1.7$–1.8 at $\beta = 0°$, while $F \simeq 1$ at $\beta \simeq 30°$, which corresponds to focused (or forward-scattering) paths (MS1, MS2 and MS3 in Fig. 1) and near-focused paths that contribute significantly to the EXAFS.

This chapter will address the basics of the EXAFS theory behind the multiple-scattering contributions, introduce strategies for their quantitative analysis, offer ideas for modelling of local structure based on the multiple-scattering contributions, and present examples and applications.

2. History and derivation

The multiple-scattering theory was rapidly developed from the early 1970s and many efforts have been made to solve this problem using different approaches (Ashley & Doniach, 1975; Lee & Pendry, 1975; Schaich, 1973). In the work of Lee and Pendry, the formalism of single-scattering and multiple-scattering paths was developed using a wavefunction approach. They also demonstrated that the Green's function method (Ashley & Doniach, 1975; Schaich, 1973) yields identical results. The major convenience of the multiple-scattering theory for data-analysis applications is that the multiple-scattering paths are classified by the total path lengths (or, for better compatibility with the real-space distances, by the half path lengths). Hence, they contribute to different spectral regions in r-space, depending on their half path length, just like the single-scattering paths, and thus can be interpreted and analyzed using the same Fourier transform methods. The
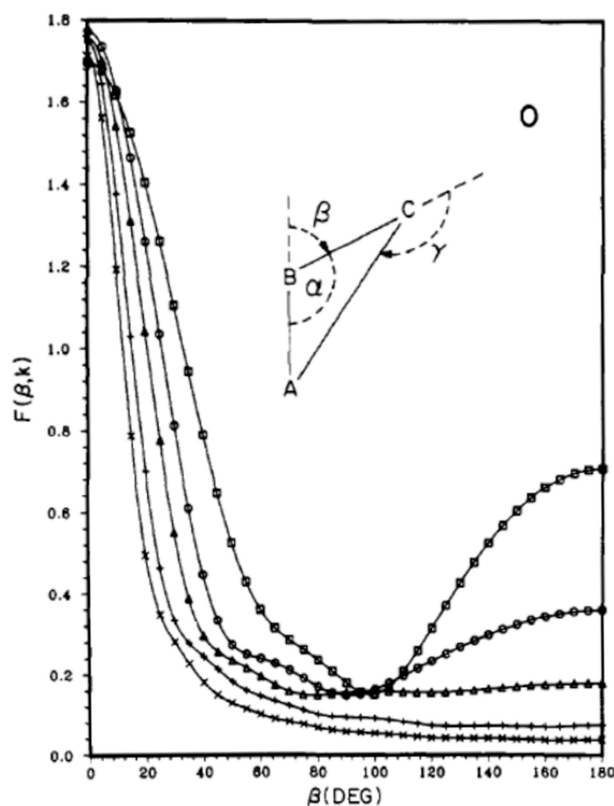
multiple-scattering expansion in terms of the one-electron Green's function in real space, known as the real-space multiple-scattering (RSMS) approach, significantly simplified the problem by avoiding the explicit calculation of final states and eigenvalues (Rehr & Albers, 2000; Rehr et al., 2002). A great research effort has been dedicated to improving the real-space full-potential multiple-scattering theory (Natoli et al., 1986, 2012). Other significant improvements in the theoretical calculation of EXAFS (Rehr & Albers, 2000) include the spherical wave approximation for scattering terms and the effective treatment of intrinsic losses, many-body and exchange correlations that are used to more accurately describe EXAFS. More recently, the Rehr–Albers approach, which is based on separable representation of Green's function propagators (Rehr & Albers, 1990), was developed to overcome the computational difficulties in the multiple-scattering expansion. With these advances, the multiple-scattering formulation of EXAFS can now be regarded as a fairly well understood problem.

The XAFS theory generally starts from Fermi's golden rule, where the contribution to the X-ray absorption coefficient from a core state is related to the transition rate of the electrons between the initial and final states,

$$\mu(E) \propto \sum_{\mathrm{f}} |\langle \psi_{\mathrm{f}} | \mathbf{p} \cdot \mathbf{A} | \psi_{\mathrm{i}} \rangle|^2 \delta(E_{\mathrm{f}} - E_{\mathrm{i}} - \hbar\omega). \qquad (1)$$

Figure 1
Representative single-scattering (SS) and multiple-scattering (MS) paths. Adapted with permission from Frenkel et al. (2001). Copyright (2001) American Chemical Society.

Figure 2
Scattering amplitude $F(\beta, k)$ (A) versus scattering angle β (°) for oxygen at different k values ranging from 3.78 to 15.12 Å^{-1}. Inset: schematic representation of a three-atom ABC system. Adapted with permission from Teo (1981). Copyright (1981) American Chemical Society.

ψ_i and ψ_f represent the wavefunctions of the excited electron for the initial and final eigenstates of the effective one-electron Hamiltonians, with energies E_i and E_f, respectively. ψ_f is calculated using the final-state one-particle Hamiltonian ('final-state rule'). The final-state one-particle Hamiltonian consists of the kinetic energy of photoelectrons, the Coulomb potential (V'_{coul}) and the photoelectron self-energy [$\Sigma(E)$]. The muffin-tin approximation used in EXAFS calculations refers to a spherical scattering potential centred on each atom and having a constant value in the interstitial region between atoms. With the separation of the potential to local scattering potentials from each atom, the muffin-tin approximation gives $\sum_{\mathbf{R}} v_{\mathbf{R}}(\mathbf{r} - \mathbf{R}) = V'_{\text{coul}} + \Sigma(E)$, with a finite range (defined by the muffin-tin radius) of scattering potentials. It has been demonstrated that the muffin-tin approximation is adequate for the theoretical simulation of EXAFS and for the analysis of experimental data. $\mathbf{p}$ is the momentum operator of the electron. $\mathbf{A}$ is the vector potential of the incident electromagnetic field and $\mathbf{A} \cong \hat{\varepsilon} A_0 \exp(i\boldsymbol{\kappa} \cdot \mathbf{r})$.

Employing the dipole approximation [$\exp(i\boldsymbol{\kappa} \cdot \mathbf{r}) \cong 1$], equation (1) becomes

$$\mu(E) \propto \sum_f \langle \psi_i | \hat{\varepsilon} \cdot \mathbf{r}' | \psi_f \rangle \delta(E_f - E_i - \hbar\omega) \langle \psi_f | \hat{\varepsilon} \cdot \mathbf{r} | \psi_i \rangle. \quad (2)$$

Considering real space, $G(\mathbf{r}, \mathbf{r}'; E)$ has the spectral representation

$$G(\mathbf{r}, \mathbf{r}'; E) = \sum_n \frac{\psi_f(\mathbf{r}')\psi_f^*(\mathbf{r})}{E - E_f + i\Gamma}, \quad (3)$$

where Γ is the core-hole lifetime, and when $\Gamma \to 0^+$

$$\left(-\frac{1}{\pi}\right)\text{Im}G(E) = \sum_f |\psi_f\rangle\delta(E - E_f)\langle\psi_f|. \quad (4)$$

Finally, the X-ray absorption coefficient is rewritten as

$$\mu = -\frac{1}{\pi}\text{Im}\langle\psi_i|\hat{\varepsilon} \cdot \mathbf{r}G(\mathbf{r}, \mathbf{r}'; E)\hat{\varepsilon} \cdot \mathbf{r}|\psi_i\rangle\theta_\Gamma(E - E_F). \quad (5)$$

where $E = E_i + \hbar\omega$ and $\theta_\Gamma(E - E_F)$ is a broadened step function at the Fermi energy with a nonzero value only when $E > E_F$.

The Green's function can be separated into intra-atomic contributions from the central (absorbing) atom G^c and multiple-scattering contributions from the environment G^{sc}, so that $G = G^c + G^{sc}$. G^{sc} can be expressed as a sum over all multiple-scattering paths. Using multiple-scattering expansion in terms of the free-particle Green's function G_0 and scattering T matrix, this yields

$$G^{sc} = G_0 T G_0 + G_0 T G_0 T G_0 + \ldots. \quad (6)$$

In equation (6), G_0 is a spherical wave, for which it is known that the longer scattering paths oscillate with higher frequency but have smaller amplitude than the shorter paths. T-matrix elements $t_{Li,L'i'} = \delta_{i,i'}\delta_{L,L'}t_l$ include all repeated scatterings within a given atomic cell. The index i denotes the atomic site in the cluster and l is the orbital angular momentum index.

An important advance in multiple-scattering theory is the approach developed by Rehr & Albers (1990, 2000) that is based on a rapidly convergent separable representation of the electron propagator, which permits fast, accurate calculations of any multiple-scattering path.

For an N-leg path that can be either single or multiple scattering, the XAFS amplitude is expressed as

$$\chi_\Gamma(p) = \text{Im}S_0^2 \frac{\exp[i(\rho_1 + \rho_2 + \ldots + \rho_N + 2\delta_1)]}{\rho_1\rho_2\ldots\rho_N}$$

$$\times \exp\left(\frac{-\sigma_\Gamma^2 p^2}{2}\right)\text{Tr}M_l F^N \ldots F^2 F^1. \quad (7)$$

M_l is a termination matrix for the final state of angular momentum, F^i is the scattering matrix at site i, $\boldsymbol{\rho}_i = p(\mathbf{R}_i - \mathbf{R}_{i-1})$, $p = (E - V_{\text{mt}})^{1/2} = (k^2 + k_F^2)^{1/2}$ is the photoelectron momentum measured with respect to the muffin-tin zero (in Rydberg atomic units), S_0^2 is a many-body reduction factor and σ_Γ^2 is the mean-square variation in total path length R_{total}.

Finally, the standard EXAFS equation, originally proposed by Sayers, Stern and Lytle (Sayers *et al.*, 1971), can be recast using the effective scattering amplitude f_{eff},

$$\chi(k) = \sum_j \frac{S_0^2 N_j}{k R_j^2}|f_{\text{eff}}(k)| \exp(-2\sigma_j^2 k^2)$$

$$\times \exp\left(-\frac{2R}{\lambda_k}\right)\sin(2k_j R + \Phi_k). \quad (8)$$

In this equation, k is the photoelectron wavenumber and f_{eff} is the effective scattering amplitude. R is defined as the effective path length and equals half the total path length ($R_{\text{total}}/2$) instead of the interatomic distance in single-scattering theory. N is the degeneracy of the scattering paths. σ^2 is known as the EXAFS Debye–Waller factor that reduces the intensity of EXAFS oscillations at high k as a consequence of disorder in interatomic distances. It is the mean-square deviation of the effective path length ($R_{\text{total}}/2$), which includes effects due to thermal variations and possible structural disorder. Φ_k is a phase function that takes into account the varying potential field along which the photoelectron moves. λ_k is the energy-dependent XAFS mean free path. The amplitude-reduction factor S_0^2 describes the intrinsic losses upon excitation which arise due to many-body effects in the photoabsorption process.

3. Data analysis

3.1. History of the *FEFF* approach

In recent decades, there have been a number of major developments in the theoretical calculation of XANES and EXAFS, in part due to advances in multiple-scattering theory. The *FEFF* code (*FEFF*3 through *FEFF*9; Rehr & Albers, 2000; Rehr *et al.*, 1991, 2009; Kas *et al.*, 2020), named after the effective scattering amplitude f_{eff}, is one of the most widely used theoretical calculation packages. In *FEFF*, the multiple-scattering calculation is based on the separable representation of the photoelectron propagator that sums over scattering paths with no conceptual distinction between single- and multiple-scattering paths. The utilization of the efficient multiple-scattering path filters and a fast path-generation and

sorting algorithm (Zabinsky *et al.*, 1995) in the *FEFF* program that eliminates paths with negligible contribution solves the path-proliferation problem.

The *FEFF* approach is based on the real-space multiple-scattering (RSMS) method within the quasiparticle picture. The RSMS approach has been widely used in calculation of the XANES and EXAFS region. The earliest version of *FEFF* (Rehr *et al.*, 1986, 1991) only included *ab initio* single-scattering XAFS calculations and was subsequently improved to involve multiple-scattering effects (Rehr & Albers, 1990; Rehr *et al.*, 1991). The latest version 9 (Ahmed *et al.*, 2012; Rehr *et al.*, 2009, 2010; Kas *et al.*, 2020) features efficient *ab initio* models including a many-pole model of the self-energy, inelastic losses and multiple-electron excitations, a linear response approach for the core hole and a Lanczos approach for Debye–Waller effects, and yields improved calculations of both EXAFS and XANES. It is also able to calculate EELS and NRIXS spectra, which were not available in previous versions.

3.2. Data-analysis procedure using *FEFF*

EXAFS data analysis can be performed by a number of software packages. Here, we use *FEFF* and *IFEFFIT* as examples to illustrate the analysis procedure. To generate the path list with the evaluated path parameters as implemented in *FEFF*, the procedure starts by constructing a model of atomic positions in three dimensions (Bunker, 2010; Newville *et al.*, 1995). The scattering paths are then constructed. The number of paths is restricted by the 'path filters', so that only multiple-scattering paths with an amplitude larger than a given cutoff value are retained. The physically equivalent paths are sorted in order of the increased half-path length and are filtered. For each path, the values of the parameters (referred to in the standard EXAFS equation) effective scattering amplitude f_{eff}, mean free path λ_k and phase shift are obtained from the *FEFF* calculation for each value of the k-grid. The changes in energy origin ΔE_0, NS_0^2, ΔR, σ^2 and the third and fourth cumulants of the effective pair distribution function are available for analysis as adjustable (or fixed)

parameters for each path to be used in the fitting of experimental data. *FEFF* calculations face a complication when dealing with some statistically or thermally disordered systems with many non-equivalent atomic sites that make it impractical to include distant multiple-scattering paths due to the large number of fitting parameters. Thus, an alternative 'direct modelling' approach, in which EXAFS spectra are simulated on the basis of molecular-dynamics simulations, has been utilized to overcome this limitation (D'Angelo *et al.*, 2002; Kuzmin & Chaboy, 2014; Vila *et al.*, 2008).

Following the *FEFF* calculation, the output of the *FEFF* program can be incorporated into an independent data-analysis program (*i.e. IFEFFIT*) for data fitting. The experimental data first have to be converted from the measured $\mu(E)$ to $\chi(k)$ by normalization and background subtraction. The experimental $\chi(k)$ in the range of interest is then Fourier transformed in a selected k-range window, so that information outside the range of interest can be ignored. In this way, the frequency of the oscillations in EXAFS can be quantitatively related to the distances between the absorbing atom and the atoms within a given coordination shell around it, as shown in Fig. 3. A weighting factor (either k, k^2 or k^3) is applied to emphasize (or de-emphasize) a particular part of the k-range in the data. The Levenberg–Marquardt nonlinear least-squares algorithm is employed in most of the commonly used programs to fit the theoretical EXAFS spectrum to the experimental data.

As mentioned in Section 1, amongst the various types of multiple-scattering paths, the forward-scattering (also known as focusing or shadowing) paths are particularly important in EXAFS data analysis. Forward scattering refers to scattering along a collinear pathway in the forward direction (with zero scattering angle). In fact, the effective path length $R = R_{\mathrm{path}}/2$ for a forward-scattering path is the same as for the corresponding single-scattering path connecting the end atoms of the linkage. The EXAFS Debye–Waller factor is defined as the mean-square deviation of the half-length of the photoelectron path from the average. It accounts for the radial disorder, but is much less sensitive to variations in the scattering angle (Kuzmin & Chaboy, 2014; Kuzmin *et al.*, 1993). In materials
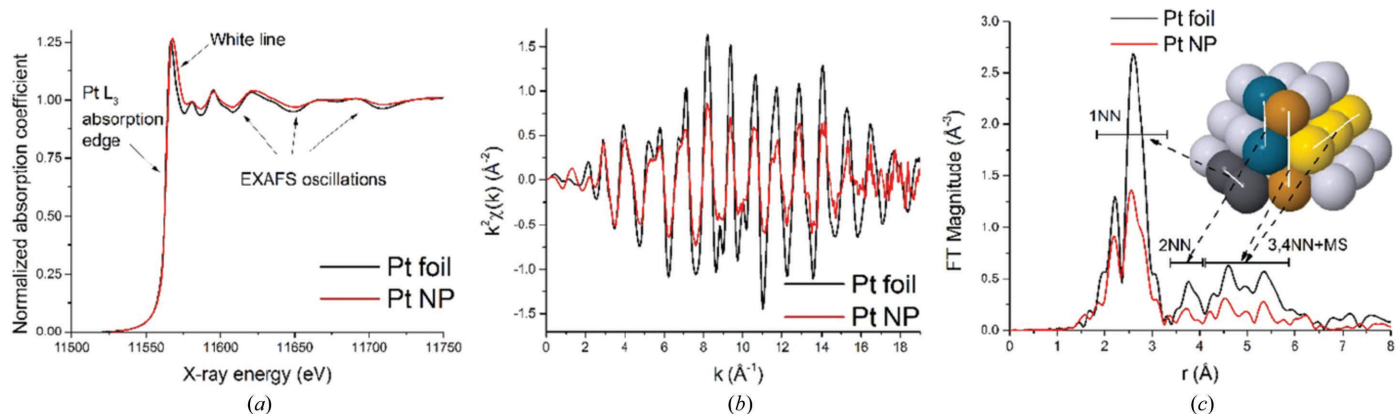
Figure 3
Raw EXAFS data for platinum nanoparticles supported on high-surface-area γ-Al$_2$O$_3$ substrate and bulk platinum (*a*) in energy, (*b*) in k-space and (*c*) in r-space. The inset in (*c*) shows a model of a truncated cuboctahedral cluster and different groups of atomic arrangements that contribute to different peaks in r-space. Reprinted with permission from Frenkel *et al.* (2014). Copyright (2014) American Vacuum Society.

with long-range periodicity, it can be related to the local displacements $\mathbf{u}_i$ from the average lattice sites. For any scattering path, the EXAFS Debye–Waller factor can be expressed as (Frenkel, 2015; Shanthakumar *et al.*, 2006)

$$\sigma_j^2 \equiv \langle (r_j - R_j)^2 \rangle = \left\langle \left[\frac{1}{2} \sum_{i=1}^{n_j} (\mathbf{u}_i - \mathbf{u}_{i+}) \hat{R}_{ii+} \right]^2 \right\rangle$$

$$= \frac{1}{4} \left\langle \left[\sum_{i=1}^{n_j} (\mathbf{u}_i - \mathbf{u}_{i+}) \hat{R}_{ii+} \right]^2 \right\rangle, \quad (9)$$

where, following the notation of Poiarkova & Rehr (1999), each leg of the path connecting instantaneous atomic positions is given by the vector $\mathbf{r}_{ii+} = \mathbf{R}_{ii+} + \mathbf{u}_{i+} + \mathbf{u}_i$, as shown in Fig. 4. $i+$ indicates the next-neighbour atom to i in the direction of the path and $\mathbf{R}_{ii+}$ and $\mathbf{u}_i$ correspond to the average leg vector and atomic displacement vector, respectively.

For a forward-scattering path, the corresponding Debye–Waller factor σ_{FW}^2 is given by

$$\sigma_{FW}^2 = \sigma_{ss}^2 = \langle u_{0x}^2 \rangle^2 + \langle u_{1x}^2 \rangle^2 - \langle 2u_{0x}u_{1x} \rangle. \quad (10)$$

Thus, the path length and Debye–Waller factor of the forward-scattering path in fitting EXAFS can be defined as the same value as the corresponding single-scattering path. In addition, it is also observed that in a highly symmetrical structure the path degeneracy changes the importance of paths even for the weaker nonlinear scattering. As seen in the case of metallic copper (Rehr & Albers, 1990), triangular paths with large degeneracy are also important and can be comparable in importance to the forward-scattering paths. In some cases of highly disordered systems, such as asymmetrically distorted nanoparticles, equation (10) is no longer valid (Frenkel, 2015). To solve this problem, direct modelling approaches based on density-functional theory and molecular dynamics have been developed (D'Angelo *et al.*, 2002; Price *et al.*, 2012; Tse, 2002; Vila *et al.*, 2008; Yancey *et al.*, 2013).

In order to evaluate the quality of fitting results, the R factor and reduced χ^2 (χ_ν^2) are often used. The R factor is an indicator of the percentage misfit to the data. It has to be interpreted carefully by checking whether the fitted parameters are

physically meaningful. The reduced χ^2 is given by $\chi_\nu^2 = \chi^2/\nu$. Here,

$$\chi^2 = \frac{N_{idp}}{N} \sum_{i=1}^{N} \left[\frac{\chi_{data}(k_i) - \chi_{model}(k_i)}{\varepsilon_i} \right]^2, \quad (11)$$

where $[\chi_{data}(k_i) - \chi_{model}(k_i)]$ is the difference between the experimental data and calculation at each point i, and ε_i is the root-mean-square uncertainty of experimental data $\chi_{data}(k_i)$. The number of degrees of freedom in the fit $\nu = N_{idp} - N_{var}$, where N_{var} is the number of variables evaluated in the fit. The number of relevant independent data points is $N_{idp} \simeq (2/\pi)\Delta R \Delta k$ [ΔR is the fitting range in R-space and Δk is the k-range of the experimental $\chi(k)$]. The reduced χ^2 allows a comparison of the quality between different fits for the same data because the χ_ν^2 value decreases when the fitting improves.

3.3. Alternative approaches

Alternative methods to the path-by-path approach adopted by *FEFF* have also been developed, for example *EXCURVE* (Gurman *et al.*, 1984, 1986; Feiters *et al.*, 2020) and *GNXAS* (Filipponi *et al.*, 1995, 2020; Westre *et al.*, 1995). The name *GNXAS* is derived from g_n (the *n*-body distribution function) and X-ray absorption spectroscopy (Filipponi *et al.*, 1995; Westre *et al.*, 1995). *EXCURVE* (exact, curved-wave approach) was the first code for EXAFS analysis, and has more recently been updated to the *DL_EXCURV* package. It comes with a ligand database and is well suited to users from the biological community. The *GNXAS* approach performs an '*n*-body decomposition' of the Green's function. All of the multiple-scattering contributions to the absorption cross section σ for a given *n* atoms under consideration are accounted for. The EXAFS signal is expanded in terms of the irreducible *n*-body signals $\gamma^{(n)}$ that are directly calculated using a muffin-tin potential and advanced models for the energy-dependent exchange–correlation self-energy. For a two-atom system, the γ^2 function includes the single, triple and all successive odd orders of scattering contributions between the absorber and scatterer, which are equivalent to the sum of all of the filtered paths calculated by *FEFF*. Practically, the lower order ($n \leq 4$) $\gamma^{(n)}$ within the first few coordination shells are usually

(a)   (b)
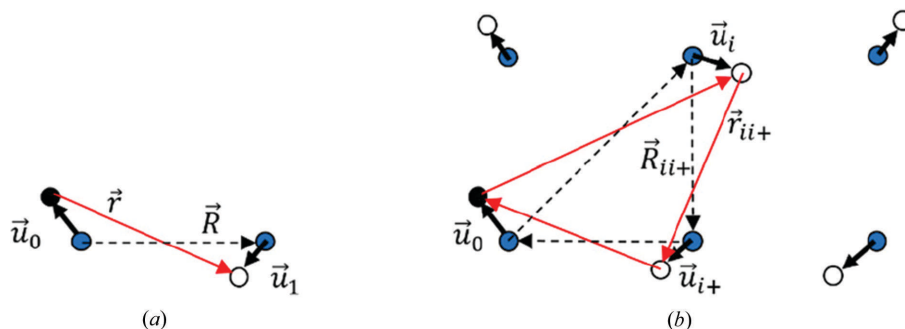
Figure 4
Illustration of the local deviations from the average atomic positions in a lattice and their relationships to the lengths of the single-scattering (*a*) and multiple-scattering (*b*) photoelectron paths. Blue circles indicate periodic lattice sites. Black circles are X-ray absorbing atoms. Open circles are instantaneous positions of atoms that are displaced from the average lattice sites due to either dynamic or static disorder or both. Reprinted from Frenkel (2015). Copyright The Royal Swedish Academy of Sciences. Reproduced by permission of IOP Publishing. All rights reserved.

accounted for. EXAFS data are then fitted using the calculated $\gamma^{(n)}$ modified by the parameters of the coordination environment. This expansion is found to have a better convergence rate than the MS series because each $\gamma^{(n)}$ signal accounts for an infinite number of MS terms.

4. Examples and applications

EXAFS data analysis using multiple-scattering theory has been widely applied for the structural characterization of various material systems in order to solve many different problems such as the size and shape of nanoparticles (Araujo *et al.*, 2008; Frenkel, 1999; Witkowska *et al.*, 2007), buckling angles of mixed salts (Frenkel *et al.*, 1993, 1994, 1995), the local structure of high-T_c superconductors (Han *et al.*, 2002; Haskel *et al.*, 2000, 2001; Sahiner *et al.*, 1999), structural phase transitions in perovskites (Hanske-Petitpierre *et al.*, 1991; Ravel *et al.*, 1998; Rechav *et al.*, 1993; Shanthakumar *et al.*, 2006), structural disorder of oxide cathode materials (Giorgetti *et al.*, 2006; Greco *et al.*, 2014) and determination of the geometry of proteins (Chen *et al.*, 2003; Immoos *et al.*, 2005; Rich *et al.*, 1998).

The work on resolving the structures (size and shape) of a number of platinum and platinum-based bimetallic nanoparticles by including the multiple-scattering contributions in EXAFS data analysis is a good example of the application of multiple-scattering analysis of EXAFS to nanoparticles. One study of carbon-supported Pt and PtRu nanoparticles (Frenkel, 1999) demonstrated that it is possible to analyze the structure (shape and size) of carbon-supported Pt and heteroatomic PtRu nanoparticles by taking multiple-scattering paths into account in EXAFS analysis. The reliability of size and shape determination from EXAFS analysis increases if the coordination numbers are obtained from higher shells. This study shows that a common strategy for analyzing monometallic and bimetallic nanoparticles involves first obtaining the amplitude-reduction factor from a fit to a bulk standard (for example metal foil) and then fixing it in subsequent fits to the nanoparticle data to obtain coordination numbers. In this paper, the Pt foil data were well fitted through 6 Å in R-space by adding the first five shells of single scattering and three nonlinear multiple-scattering paths in fitting. For the Pt nanoparticles, the multiple-scattering analysis allows the measurements of coordination numbers within the first four single-scattering paths and one nonlinear multiple-scattering path. As a test, the Pt nanoparticles were proved to have the shape of a hemispherical cuboctabedron with a size of 15–20 Å. The latter analysis of carbon-supported PtRu nanoparticles is performed by including four shells of single scattering and the most dominant collinear double- and triple-scattering paths. It also constrains the heterometallic bonds to have the same bond lengths and disorder parameters as viewed from either metal absorption edge. Furthermore, the coordination numbers of heterometallic bonds were fixed according to the element composition. The obtained information on local environments shows a marked preference for segregation of Pt atoms to the particle surface in the fully reduced particles. The carbon-supported PtRu nanoparticles were shown to have adopted a hemispherical cuboctahedron f.c.c. structure with an average diameter of about 15 Å. In combination with electron microscopy and electron diffraction, the EXAFS analysis of Pt and PtRu nanoparticles, considering multiple-scattering contributions, provides structural information with higher accuracy than only using the first-shell EXAFS analysis.

Similarly, in the case of Pt nanoparticles on a γ-Al_2O_3 support (measured under a 2.5% CO/97.5% He flow at room temperature; Frenkel *et al.*, 2014), the peak positions are correlated with the pair distribution function peaks that correspond to the first, second, third *etc.* coordination shells, although for higher order shells such determination is difficult due to the contribution of multiple-scattering paths in the same r-range as single-scattering paths of the same length (Fig. 4). In the EXAFS analysis of 4.0 nm Ru@Pt core-shell nanoparticles (NPs; Alayoglu *et al.*, 2009), the structural parameters of the Pt shell were extracted beyond the first coordination shell by including the multiple-scattering contributions in the *FEFF* analysis of Ru@Pt NPs, while for the Ru K edge such a higher order contribution is absent due to the poorly ordered core structure (Fig. 5). The EXAFS results revealed that the Ru@Pt core-shell NPs consist of a highly disordered Ru core and a relatively crystalline Pt shell, which is consistent with XRD and TEM studies.

Besides the size and shape determination of nanomaterials, the multiple-scattering contributions from forward or nearly collinear scattering paths in EXAFS were also used to reveal the r.m.s. buckling angle of mixed salts from the average NaCl structure (Frenkel *et al.*, 1993, 1994, 1995). In the perfect NaCl structure, the collinear double-scattering (DS) and triple-scattering (TS) paths in the distant R range, containing the first nearest neighbour as the focusing atom, are enhanced compared with the single-scattering path with the same path length. This effect is very sensitive to the angular deviation from collinearity in these paths and can be used to measure it as long as it is smaller than 20°. In a mixture $A_xB_{1-x}C$ of salts AC and BC with composition x and choosing C as the absorbing atom, the root-mean-square (r.m.s.) values of the buckling angles, described as $\Theta_1 = 180° - \widehat{CAC'}$ and $\Theta_2 = 180° - \widehat{CBC'}$, could be determined from fits that employ the DS and TS paths. The forward-scattering amplitude F of the focusing atom in these paths has a maximum when the atoms are collinear ($\Theta = 0$), as demonstrated above. Polynomial expansion of $F(k, \Theta)$ has its lowest order of Θ^2 in the vicinity of $\Theta = 0$. Averaging over the total number of absorbing atoms, one obtains

$$\langle F(k, \Theta)\rangle \simeq F(k, 0)[1 - b(k)\langle\Theta^2\rangle]. \qquad (12)$$

The forward-scattering amplitude $F(k, 0)$ for the intervening atom in the three-atom linkage is determined by *FEFF* calculations on the ordered structure of the corresponding pure salts. $F(k, \Theta)$ is calculated by *FEFF* for DS paths with the focusing atom moving out of the collinear position according to the predefined Θ values. The curvature coefficient $b(k)$ is then found by the fit to equation (11) in a small Θ range (up to
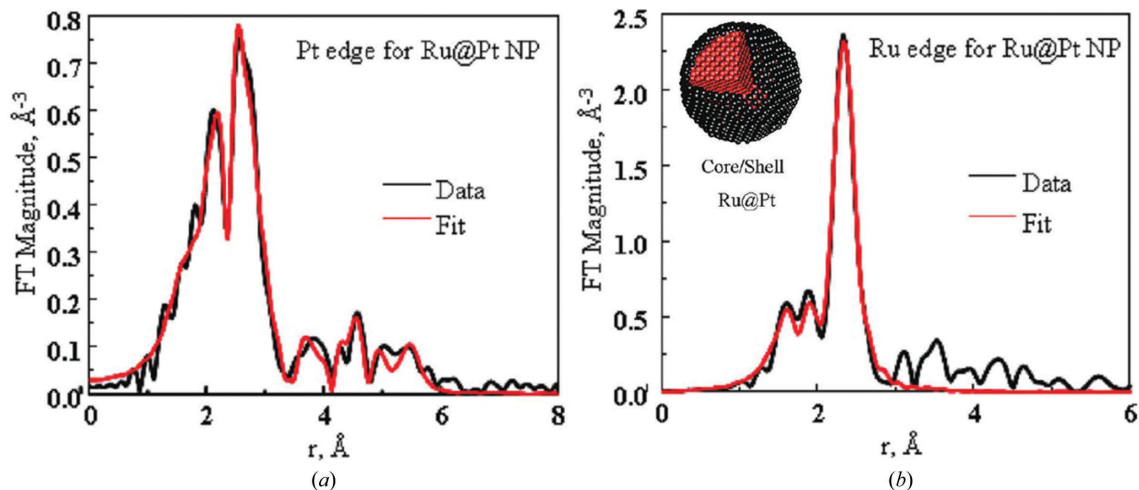
Figure 5
Fourier transform magnitudes of the *FEFF*6 theory (red) to the EXAFS data at (*a*) the Pt L_3 edge and (*b*) the Ru K edge for Ru@Pt core-shell NPs. The model structure of the Ru@Pt core-shell NP is shown as an inset. Adapted with permission from Alayoglu *et al.* (2009). Copyright (2009) American Chemical Society.

$20°$). One can approximate the process further by fixing the value of $b(k)$ at a constant; Θ^2 can then be refined as a new amplitude correction in the fit of EXAFS data. Applying the EXAFS fitting using the above strategy, the r.m.s. buckling angles in the mixed salts $Rb_{0.76}K_{0.24}Br$ and $RbBr_{0.62}Cl_{0.38}$ were obtained as $7–9°$ (Frenkel *et al.*, 1994).

Angular-dependent XAFS measurements were used to study local disorder in the structure of high-temperature superconductors (Han *et al.*, 2002; Haskel *et al.*, 2000, 2001). One of the challenges is to determine the orientation of CuO_6 octahedra, which differs between the bulk structures of different phases in Li_2CuO_4 materials [for example low-temperature tetragonal (LTT), low-temperature ortho-rhombic (LTO) and high-temperature tetragonal (HTT)]. Using the case of $La_{2-x}Ba_xCuO_4$ ($x = 0.125, 0.15$) (Haskel *et al.*, 2000) as an example, the local tilt angle of CuO_6 octahedra was determined by the buckling angle of the collinear multiple-scattering path La–O–Cu obtained from analysis of the La K-edge EXAFS data. The buckling angles obtained from the EXAFS data fitting were the same as in the LTT configuration and were found to be nearly temperature-independent. These results suggest that the local tilts of CuO_6 octahedra remain the same as in the LTT phase, which is evidence of a significant order–disorder contribution to the mechanism of phase transitions in $La_{2-x}Ba_xCuO_4$ ($x = 0.125$, 0.15).

Another good example is the multiple-scattering EXAFS analysis of tetraalkylammonium (TAA) manganese oxide colloids (Ressler *et al.*, 1999). Two series of colloidal TAA MnO_x prepared with tetrapropylammonium (TPA) and tetraethylammonium (TEA) cations were studied. EXAFS analysis was carried out to distances of 6 Å around the central Mn atom using the single-scattering, collinear forward-scattering, selected triangular and higher order scattering paths. Differences in the refined scattering shell distances between the TPA and TEA series suggest a structure-influencing effect of the two ammonium ions. Bond angles between neighbouring MnO_6 octahedra were determined from the amplitude dependence of a collinear Mn–Mn–Mn forward-scattering path. Based on the obtained bond angles and the assumption of a certain degree of ordering of trivalent and tetravalent manganese in the MnO_x layers, three distinct 2D structures are proposed: one for birnessite, one for TAA sols and one for TAA gels.

5. Conclusions and outlook

The multiple-scattering theory of EXAFS has rapidly been developed in the past few decades. The computational codes and software based on multiple-scattering theory have become very efficient and useful tools for calculating and interpreting EXAFS data. The science community in many fields, including catalysts (Frenkel, 2012, 2015; Frenkel *et al.*, 2014), batteries (Giorgetti, 2013), biology (Charnock, 1995; Parsons *et al.*, 2002), semiconductor heterostructures (Boscherini, 2008), ferroelectric materials (Cabrera, 2011) and so on (Wende, 2004; Kuzmin & Chaboy, 2014; Sun *et al.*, 2013), have greatly benefited from the utilization of multiple-scattering analysis of EXAFS. However, in some cases of low-symmetry or amorphous systems, it is not necessary to apply the multiple-scattering analysis of EXAFS since the multiple-scattering contributions are very weak and can be neglected. As the EXAFS information is limited to the nearest environment of absorbing atoms, complementary characterization techniques, such as X-ray diffraction and electron microscopy, are usually employed in conjunction with XAFS to provide 3D structural information on the materials.

As mentioned earlier, although multiple-scattering theory in EXAFS has been well established, there is potential to improve the accuracy of calculation in general; for example, corrections to the muffin-tin potential approximation and a better treatment of inelastic losses and disorder may potentially enhance the accuracy of calculation (Rehr & Albers, 2000).

References

Ahmed, T., Kas, J. J. & Rehr, J. J. (2012). *Phys. Rev. B*, **85**, 165123.

Alayoglu, S., Zavalij, P., Eichhorn, B., Wang, Q., Frenkel, A. I. & Chupas, P. (2009). *ACS Nano*, **3**, 3127–3137.

Araujo, L. L., Foran, G. J. & Ridgway, M. C. (2008). *J. Phys. Condens. Matter*, **20**, 165210.

Ashley, C. A. & Doniach, S. (1975). *Phys. Rev. B*, **11**, 1279–1288.

Balerna, A., Bernieri, E., Burattini, E., Kuzmin, A., Lusis, A., Purans, J. & Cikmach, P. (1991). *Nucl. Instrum. Methods Phys. Res. A*, **308**, 234–239.

Boscherini, F. (2008). *Characterization of Semiconductor Heterostructures and Nanostructures*, pp. 289–330. Amsterdam: Elsevier.

Bunker, G. (2010). *Introduction to XAFS.* Cambridge University Press.

Cabrera, M. E. M. (2011). *Multifunctional Polycrystalline Ferroelectric Materials: Processing and Properties*, pp. 281–346. Dordrecht: Springer.

Charnock, J. M. (1995). *Radiat. Phys. Chem.* **45**, 385–391.

Chen, K., Yuldasheva, S., Penner-Hahn, J. E. & O'Halloran, T. V. (2003). *J. Am. Chem. Soc.* **125**, 12088–12089.

D'Angelo, P., Barone, V., Chillemi, G., Sanna, N., Meyer-Klaucke, W. & Pavel, N. V. (2002). *J. Am. Chem. Soc.* **124**, 1958–1967.

Feiters, M. C., Strange, R. W. & Binsted, N. (2020). *Int. Tables Crystallogr. I*, https://doi.org/10.1107/S1574870720003262.

Filipponi, A., Di Cicco, A. & Natoli, C. R. (1995). *Phys. Rev. B*, **52**, 15122–15134.

Filipponi, A., Natoli, C. R. & Di Cicco, A. (2020). *Int. Tables Crystallogr. I*, https://doi.org/10.1107/S1574870720003286.

Frenkel, A. I. (1999). *J. Synchrotron Rad.* **6**, 293–295.

Frenkel, A. I. (2012). *Chem. Soc. Rev.* **41**, 8163–8178.

Frenkel, A. I. (2015). *Phys. Scr.* **90**, 098004.

Frenkel, A. I., Cason, M. W., Elsen, A., Jung, U., Small, M. W., Nuzzo, R. G., Vila, F. D., Rehr, J. J., Stach, E. A. & Yang, J. C. (2014). *J. Vac. Sci. Technol. A*, **32**, 020801.

Frenkel, A. I., Hills, C. W. & Nuzzo, R. G. (2001). *J. Phys. Chem. B*, **105**, 12689–12703.

Frenkel, A., Stern, E. A., Voronel, A., Qian, M. & Newville, M. (1993). *Phys. Rev. Lett.* **71**, 3485–3488.

Frenkel, A., Stern, E. A., Voronel, A., Qian, M. & Newville, M. (1994). *Phys. Rev. B*, **49**, 11662–11674.

Frenkel, A., Voronel, A., Katzir, A., Newville, M. & Stern, E. A. (1995). *Physica B*, **208–209**, 334–336.

Giorgetti, M. (2013). *ISRN Mater. Sci.* **2013**, 938625.

Giorgetti, M., Berrettoni, M., Scaccia, S. & Passerini, S. (2006). *Inorg. Chem.* **45**, 2750–2757.

Greco, G., Brutti, S., Vitucci, F. M., Lombardo, L., Köntje, M., Savoini, A., Paolone, A. & Panero, S. (2014). *J. Phys. Chem. C*, **118**, 26471–26478.

Gurman, S. J., Binsted, N. & Ross, I. (1984). *J. Phys. C. Solid State Phys.* **17**, 143–151.

Gurman, S. J., Binsted, N. & Ross, I. (1986). *J. Phys. C. Solid State Phys.* **19**, 1845–1861.

Han, S.-W., Stern, E. A., Haskel, D. & Moodenbaugh, A. R. (2002). *Phys. Rev. B*, **66**, 094101.

Hanske-Petitpierre, O., Yacoby, Y., Mustre de Leon, J., Stern, E. A. & Rehr, J. J. (1991). *Phys. Rev. B*, **44**, 6700–6707.

Haskel, D., Stern, E. A., Dogan, F. & Moodenbaugh, A. R. (2000). *Phys. Rev. B*, **61**, 7055–7076.

Haskel, D., Stern, E., Dogan, F. & Moodenbaugh, A. R. (2001). *J. Synchrotron Rad.* **8**, 186–190.

Immoos, C. E., Sulc, F., Farmer, P. J., Czarnecki, K., Bocian, D. F., Levina, A., Aitken, J. B., Armstrong, R. S. & Lay, P. A. (2005). *J. Am. Chem. Soc.* **127**, 814–815.

Kas, J. J., Vila, F. D. & Rehr, J. J. (2020). *Int. Tables Crystallogr. I*, https://doi.org/10.1107/S1574870720003274.

Kuzmin, A. & Chaboy, J. (2014). *IUCrJ*, **1**, 571–589.

Kuzmin, A. & Purans, J. (1993). *J. Phys. Condens. Matter*, **5**, 2333–2340.

Kuzmin, A., Purans, J., Benfatto, M. & Natoli, C. R. (1993). *Phys. Rev. B*, **47**, 2480–2486.

Lee, P. A. & Pendry, J. B. (1975). *Phys. Rev. B*, **11**, 2795–2811.

Natoli, C. R., Benfatto, M. & Doniach, S. (1986). *Phys. Rev. A*, **34**, 4682–4694.

Natoli, C. R., Krüger, P., Hatada, K., Hayakawa, K., Sébilleau, D. & Šipr, O. (2012). *J. Phys. Condens. Matter*, **24**, 365501.

Newville, M., Ravel, B., Haskel, D., Rehr, J. J., Stern, E. A. & Yacoby, Y. (1995). *Physica B*, **208–209**, 154–156.

Parsons, J. G., Aldrich, M. V. & Gardea-Torresdey, J. L. (2002). *Appl. Spectrosc. Rev.* **37**, 187–222.

Penner-Hahn, J. E. (2001). *eLS*, https://doi.org/10.1038/npg.els.0002984.

Poiarkova, A. V. & Rehr, J. J. (1999). *Phys. Rev. B*, **59**, 948–957.

Price, S. W. T., Zonias, N., Skylaris, C.-K., Hyde, T. I., Ravel, B. & Russell, A. E. (2012). *Phys. Rev. B*, **85**, 075439.

Ravel, B., Stern, E. A., Vedrinskii, R. I. & Kraizman, V. (1998). *Ferroelectrics*, **206**, 407–430.

Rechav, B., Sicron, N., Yacoby, Y., Ravel, B., Newville, M. & Stern, E. A. (1993). *Physica C*, **209**, 55–58.

Rehr, J. J. & Albers, R. C. (1990). *Phys. Rev. B*, **41**, 8139–8149.

Rehr, J. J. & Albers, R. C. (2000). *Rev. Mod. Phys.* **72**, 621–654.

Rehr, J. J., Albers, R. C., Natoli, C. R. & Stern, E. A. (1986). *Phys. Rev. B*, **34**, 4350–4353.

Rehr, J. J., Kas, J. J., Prange, M. P., Sorini, A. P., Takimoto, Y. & Vila, F. (2009). *C. R. Phys.* **10**, 548–559.

Rehr, J. J., Kas, J. J., Vila, F. D., Prange, M. P. & Jorissen, K. (2010). *Phys. Chem. Chem. Phys.* **12**, 5503–5513.

Rehr, J. J., Mustre de Leon, J., Zabinsky, S. I. & Albers, R. C. (1991). *J. Am. Chem. Soc.* **113**, 5135–5140.

Rehr, J. J., Schattke, W., García de Abajo, F. J., Díez Muiño, R. & Van Hove, M. A. (2002). *J. Electron Spectrosc. Relat. Phenom.* **126**, 67–76.

Ressler, T., Brock, S. L., Wong, J. & Suib, S. L. (1999). *J. Phys. Chem. B*, **103**, 6407–6420.

Rich, A. M., Armstrong, R. S., Ellis, P. J. & Lay, P. A. (1998). *J. Am. Chem. Soc.* **120**, 10827–10836.

Sahiner, A., Crozier, E. D., Jiang, D. T. & Ingalls, R. (1999). *Phys. Rev. B*, **59**, 3902–3910.

Sayers, D. E., Stern, E. A. & Lytle, F. W. (1971). *Phys. Rev. Lett.* **27**, 1204–1207.

Schaich, W. L. (1973). *Phys. Rev. B*, **8**, 4028–4032.

Shanthakumar, P., Balasubramanian, M., Pease, D. M., Frenkel, A. I., Potrepka, D. M., Kraizman, V., Budnick, J. I. & Hines, W. A. (2006). *Phys. Rev. B*, **74**, 174103.

Sun, Z., Yan, W., Yao, T., Liu, Q., Xie, Y. & Wei, S. (2013). *Dalton Trans.* **42**, 13779–13801.

Teo, B.-K. (1981). *J. Am. Chem. Soc.* **103**, 3990–4001.

Teo, B.-K. & Lee, P. A. (1979). *J. Am. Chem. Soc.* **101**, 2815–2832.

Tse, J. S. (2002). *Annu. Rev. Phys. Chem.* **53**, 249–290.

Vila, F., Rehr, J. J., Kas, J., Nuzzo, R. G. & Frenkel, A. I. (2008). *Phys. Rev. B*, **78**, 121404.

Wende, H. (2004). *Rep. Prog. Phys.* **67**, 2105–2181.

Westre, T. E., Di Cicco, A., Filipponi, A., Natoli, C. R., Hedman, B., Solomon, E. I. & Hodgson, K. O. (1995). *J. Am. Chem. Soc.* **117**, 1566–1583.

Witkowska, A., Di Cicco, A. & Principi, E. (2007). *Phys. Rev. B*, **76**, 104110.

Yancey, D. F., Chill, S. T., Zhang, L., Frenkel, A. I., Henkelman, G. & Crooks, R. M. (2013). *Chem. Sci.* **4**, 2912–2921.

Zabinsky, S. I., Rehr, J. J., Ankudinov, A., Albers, R. C. & Eller, M. J. (1995). *Phys. Rev. B*, **52**, 2995–3009.